




Regge poles of analogous rotating black holes in binary Bose-Einstein condensates: The gapped excitations

Wei-Can Syu 

Center of General Education, Wenzao Ursuline University of Languages, Kaohsiung 780793, Taiwan, R.O.C.

Tien Hsieh  and Da-Shin Lee 

Department of Physics, National Dong-Hwa University, Hualien 974301, Taiwan, R.O.C.

(Dated: July 22, 2025)

In this paper, we study the spectrum of the Regge poles (RPs), which are the counterparts of quasinormal modes, in a draining bathtub vortex within a two-component Bose-Einstein condensate (BEC) system. We study the gapped excitations of the condensate with the spatially dependent energy gap term using a spatially tunable Rabi coupling, which will be treated as a perturbation. This model serves as an analogue of a rotating black hole surrounded by an environmental mass shell. We first compute the semiclassical scattering amplitude with the spatially independent mass effect due to the orbital interference. In the case of the mass-shell, bifurcation of the spectrum is observed, resulting in the destabilization of the RPs. We also study the migration of RPs by shifting the bump position. Our results show that the RPs of the co-rotating modes exhibit greater stability than those of the counter-rotating modes. Large migration and overtaking jumps of the overtone (fundamental RP) leave an imprint on the scattering amplitude at small (large) scattering angles. This can be observed in the scattering interference pattern in experiments.

I. INTRODUCTION

In general relativity (GR) linear gravitational perturbations of black hole spacetimes can be probed through their damped oscillatory behavior, giving rise to the emission of gravitational waves during the ringdown phase of a binary black hole merger. They are of particular importance today, because of their relevance to gravitational wave astronomy. The damped resonances are manifest as poles in the scattering matrix, occurring at complex frequencies and complex angular momenta. The corresponding modes are known as quasinormal mode (QNM) and Regge pole (RP), respectively [1–3]. From the perspective of RPs, they will provide a framework to establish a link between spectral instabilities and scattering quantities. Nevertheless, black holes are typically not isolated, but are surrounded by matter such as accretion disks and dark matter. Therefore, the QNM spectra that we observe from gravitational waves should be modified by interactions with their surroundings [4–9].

Recently studies in analogue gravity have focused on mimicking the geometry of a spinning black hole in $2+1$ dimensions using a draining bathtub (DBT) vortex flow [10–15]. Apart from a theoretical consideration of massless scalar fields in the analogue black hole spacetime, the massive scalar fields has also been put forward [16–22]. In particular, in Ref. [22], we consider two-component Bose-Einstein condensates (BECs) and introduce the BEC vortex in $2+1$ dimensions. The advent of experimental studies on tunable binary BECs in Refs. [23–26] makes it possible to observe these two types of excitations. Our

primary focus is on gapped excitations, in which the energy gap acts as a mass term for an analogue of relativistic scalar fields. We study superradiant instabilities resulting from the quasibound states due to positive mass squared and the tachyonic instabilities arising from negative mass squared in both the frequency and time domains. The instability can be realized through time-dependent observables. In this work, we consider RPs and explore potential spectral instabilities of gapped excitations in the presence of a rotating vortex in a DBT background. Building on the work of Refs. [27, 28], we extend it to incorporate spatially shell-like perturbations, giving rise to the mass shell of an analogous scalar field.

With the spatially dependent perturbations, the spectral instabilities are found when bifurcations of the complex angular momentum appears in the spherically symmetric spacetime [29, 30]. One of our main focuses here is the potential destabilization behavior of RPs in an analogous rotating black hole spacetime. Additionally, we apply the idea of Ref. [31] to examine the migration of RPs in response to changes in the location of the mass shell. This allows us to investigate the behavior of the bifurcation of RPs, which may undergo either large migration or the so-called overtaking jumps. The instability behavior in terms of time-independent scattering can also be reconstructed using the complex angular momentum (CAM) method.

The layout of the paper is as follows. In Sec. II, we introduce the two-component BEC system, adapted from [22], and the time-independent scattering theory. In Sec. III, the scattering amplitude is computed using a semi-classical approximation for high-frequency scattering. This provides an alternative interpretation of the scattering amplitude in terms of orbiting. In Sec. IV, the RPs of the fundamental mode and overtones are studied, revealing bifurcation of the RP spectrum when taking ac-

* syuweican@gmail.com

† dslee@gms.ndhu.edu.tw

count of the bump perturbations. Additionally, the migration trajectory and how changing the bump location affects it will be explored. Sec. V is devoted to the numerical study. In Sec. VI, the conclusions are drawn. Appendix A reviews the continued fraction method (CFM), and Appendix B provides more detailed derivations to achieve at (43).

II. SET-UP AND TIME-INDEPENDENT SCATTERING THEORY

Here, we provide a mini-review of the DBT model in two-component BECs and summarize the key equations. See [22] for more details. The binary Bose-Einstein condensates system we consider is for identical atoms with distinct internal hyperfine states, where the coupling constants can be tuned by introducing Feshbach resonances [32–35]. In addition, transitions between these two states are allowed and governed by the Rabi frequency Ω , where $\Omega \geq 0$. With the unit $\hbar = 1$ throughout this paper, the coupled time-dependent equations of motion in 2 + 1 dimensions are expressed by

$$i\partial_t \hat{\Psi}_i = \left[-\frac{1}{2m_a} \nabla^2 + V_i + g_{ii} \hat{\Psi}_i^\dagger \hat{\Psi}_i + g_{ij} \hat{\Psi}_j^\dagger \hat{\Psi}_j \right] \hat{\Psi}_i - \frac{\Omega}{2} \hat{\Psi}_j \quad (1)$$

with $i \neq j$ and $i, j = 1, 2$, where m_a is the atomic mass, and V_i are the external potentials corresponding to the hyperfine states i . The coupling constants g_{ii} and g_{ij} represent the strength of the interaction between atoms in the same hyperfine state and between atoms in different hyperfine states, respectively.

The condensate wave functions can be obtained from the expectation values of the field operator $\langle \hat{\Psi}_i \rangle$ given by, $\langle \hat{\Psi}_i \rangle(\mathbf{r}, t) = \sqrt{\rho_i(\mathbf{r}, t)} e^{i\theta_i(\mathbf{r}, t) - i\mu t}$ with the chemical potential μ . The condensate flow velocities are $\mathbf{v}_i = \nabla \theta_i / m_a$. The perturbations around the stationary wave functions can be defined through $\hat{\Psi}_i = \langle \hat{\Psi}_i \rangle (1 + \hat{\phi}_i)$, where the fluctuation fields can be written in terms of the density and the phase as $\hat{\phi}_i = \delta \hat{n}_i + i \delta \hat{\theta}_i = \frac{\delta \hat{\rho}_i}{2\rho_i} + i \delta \hat{\theta}_i$.

According to [18], the equations can be decoupled for the general spatially dependent condensate wave functions and the coupling strengths by choosing the time-independent background solutions as $\rho_1 = \rho_2 = \rho$, $\theta_1 = \theta_2 = \theta$, and $g_{11} = g_{22} = g$. We also consider a miscible state of the background condensates with the scattering parameters of $g_{12} < g$. Further linear combination between the states $\sqrt{2} \delta \hat{n}_{d/s} = \delta \hat{n}_1 \pm \delta \hat{n}_2$ and $\sqrt{2} \delta \hat{\theta}_{d/s} = \delta \hat{\theta}_1 \pm \delta \hat{\theta}_2$ giving the (gapless) density and (gapped) spin modes yields a single equation for $\delta \hat{\theta}_s$ in the form of the Klein-Gordon equation for a massive scalar field,

$$\frac{1}{\sqrt{-g}} \partial_\mu \left(\sqrt{-g} g^{\mu\nu} \partial_\nu \delta \hat{\theta}_s \right) - m_{\text{eff}}^2 \delta \hat{\theta}_s = 0, \quad (2)$$

where the acoustic metric $g^{\mu\nu}$ depends on the background density ρ and phase θ with the spatially dependent sound speed given by $c^2 = [(g - g_{12})\rho + \Omega]/m_a \simeq (g - g_{12})\rho/m_a$, and the effective mass $m_{\text{eff}}^2 = 2m_a^2 c \Omega / \rho$. In this work, we consider small perturbations given by the small Ω , which mimic the environmental effects to the dynamics of classical perturbations around black hole spacetime.

Following [15], let us build up the analogues geometry of a rotating black hole by introducing a draining vortex with the velocity flow

$$\mathbf{v} = \frac{1}{m_a} \nabla \theta = \frac{-d\mathbf{e}_r + \ell \mathbf{e}_\phi}{m_a r} = v_r \mathbf{e}_r + v_\phi \mathbf{e}_\phi, \quad (3)$$

where the winding number ℓ is taken as an integer for quantum vortices and $d > 0$ for the draining flow. In the Thomas-Fermi approximations, we consider the region far from the core of the vortex with the radius $r \gg R_{\text{TF}} = \sqrt{\frac{d^2 + \ell^2}{2m_a \rho_\infty (g + g_{12})}}$, where the density ρ can be treated as a constant [15], $\rho \simeq \rho_\infty$ given by $\rho_\infty = \frac{1}{g + g_{12}} (\mu - V_0 \pm \frac{\Omega}{2}) \simeq \frac{1}{g + g_{12}} (\mu - V_0)$ for an uniform external potential V_0 and by ignoring the small Ω , leading to a constant sound speed c^2 . Under the coordinate transformations

$$d\tilde{t} = dt - (c^2/v_r^2 - 1)^{-1} dr, \quad (4a)$$

$$d\tilde{\phi} = d\phi - \frac{v_r v_\phi}{r(c^2 - v_r^2)} dr, \quad (4b)$$

the metric becomes

$$ds^2 = \tilde{g}_{\mu\nu}^{\text{vortex}} d\tilde{x}^\mu d\tilde{x}^\nu \\ \propto - \left(1 - \frac{r_E^2}{r^2} \right) d\tilde{t}^2 + \left(1 - \frac{r_H^2}{r^2} \right)^{-1} dr^2 \\ - \frac{2\ell}{m_a} d\tilde{\phi} d\tilde{t} + r^2 d\tilde{\phi}^2 \quad (5)$$

with $\tilde{x} = (\tilde{t}, r, \tilde{\phi})$, where the acoustic horizon and the ergosphere are located at $r_H = d/m_a c$ and $r_E = \sqrt{d^2 + \ell^2}/m_a c$, respectively. The notation can be simplified by defining dimensionless variables: $r/r_H \rightarrow r$, $c\tilde{t}/r_H \rightarrow t$ and $r_H \Omega/c \rightarrow \Omega$. For convenience, we also relabel $\tilde{\phi}$ as ϕ .

Using the field of phase fluctuation of the form

$$\delta \theta_s(t, r, \phi) = \frac{H_{\omega, m}(r)}{\sqrt{r}} e^{-i\omega t + im\phi}, \quad (6)$$

the radial equation in the tortoise coordinate $r^* = r + \frac{1}{2} \log \left| \frac{r-1}{r+1} \right|$ becomes the time-independent Schrodinger-like equation

$$[\partial_{r^*}^2 + V_{\text{eff}}(r)] H_{\omega, m}(r) = 0, \quad (7)$$

where

$$V_{\text{eff}}(r) = \left(\omega - \frac{m\ell}{r^2} \right)^2 - \left(\frac{r^2 - 1}{r^2} \right) \\ \times \left[\frac{5}{4r^4} + \frac{1}{r^2} \left(m^2 - \frac{1}{4} \right) + \mu_s^2(r) \right] \quad (8)$$

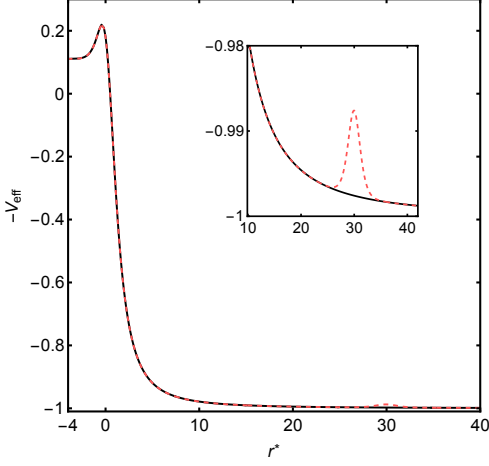


FIG. 1. The effective potential as a function of the tortoise coordinate r^* without the perturbation (black) and with the perturbation (red dashed) at $r_0 = 30$. The parameters are set to $\omega = 1$ and $\ell = 1$. The inset plot zooms in on the effective potential near the bump.

with $\mu_s^2(r) = 2d\Omega(r)$. The effective mass squared term can now be parametrized in an analytically treatable form as

$$\mu_s^2(r) = 2d\Omega(r) = \epsilon \operatorname{sech}^2[\alpha(r - r_0)], \quad (9)$$

where $\epsilon = 2d\Omega_0$, mimicking a mass shell surrounding the black hole [7, 8, 36, 37]. The profile is controlled by its typical distance from the black hole horizon and the width of the distribution. Throughout this paper, we fix the parameters as $\epsilon = 10^{-2}$, and $\alpha = 3/2$. The typical $V_{\text{eff}}(r)$ is shown in Fig. 1.

The theoretical studies of a planar wave scattered by a draining vortex has been intensely studied in Refs. [27, 28]. Here we investigate numerically the wave equation (7) where the solution obeys the boundary conditions of the pure ingoing wave at the horizon and the incoming/outgoing waves at infinity given by

$$H_{\omega,m}(r^*) \sim \begin{cases} e^{-i(\omega - m\ell)r^*}, & (r^* \rightarrow -\infty), \\ A^{\text{out}} e^{i\omega r^*} + A^{\text{in}} e^{-i\omega r^*}, & (r^* \rightarrow \infty). \end{cases} \quad (10)$$

The scattering amplitude is given by

$$f_\omega(\phi) = \sqrt{\frac{1}{2i\pi\omega}} \sum_{m=-\infty}^{\infty} (e^{2i\delta_m} - 1) e^{im\phi} \quad (11)$$

with the phase shift defined as

$$e^{2i\delta_m} = i(-1)^m A^{\text{out}}/A^{\text{in}}. \quad (12)$$

The differential cross section is obtained from the scattering amplitude as

$$\frac{d\sigma}{d\phi} = |f_\omega(\phi)|^2. \quad (13)$$

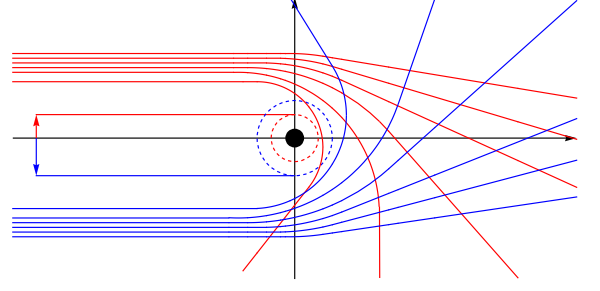


FIG. 2. Schematic diagram of the particle scattering with the interference. The spin of the black hole is clockwise. The red solid line represents the co-rotating orbits, while the blue solid line corresponds to the counter-rotating orbits.

For a real-valued frequency ω and with the pure outgoing wave $e^{i\omega r^*}$ at infinity, namely $A^{\text{in}} = 0$, the resonances occur with the complex value $m = \operatorname{Re} m + i\operatorname{Im} m$ for the RPs, with which to compute the time-independent scattering amplitude.

III. DIFFERENTIAL SCATTERING CROSS SECTION IN SEMICLASSICAL APPROXIMATIONS

In classical scattering, the differential cross section for a given scattering angle can be associated with a specific scattering orbit. However, in quantum mechanics, the wave properties will lead to the fact that the differential cross section is the square modulus of the scattering amplitude, which is computed as the sum of wavefunctions that scatter into a particular angle. Before computing the full quantum mechanical scattering amplitude, we begin by studying its classical scattering cross section obtained from geodesic dynamics in the effective rotating black hole spacetime. The contributions of the geodesics to the cross section with the interference effects in the semiclassical approximation [38, 39] will show the characteristic properties of the full quantum mechanical scattering amplitude suited for the relatively high frequency scattering.

Below, we will follow the semiclassical analysis in Ref. [28] but extend it by including the perturbation to the null geodesics arising from an effective small spatially independent mass term, which is theoretically treatable. We consider high energy scattering, which the energy is of order of the inverse of the characteristic length scale of the analog rotating spacetime, the ergosphere radius, such that $E \propto 1/r_E \gg \sqrt{\epsilon}$. In an asymptotic regime, the energy can be safely approximated by $E^2 = \omega^2 + \epsilon^2 \approx \omega^2$.

However, the geodesics equation, governing the orbits toward an asymptotic regime, is perturbed by the mass term to be $g_{\mu\nu} p^\mu p^\nu = -m^2 \equiv -\epsilon$. For small perturbations, the scattering orbit will be perturbed and result in the slightly change in the deflection angle. Then, in the semiclassical approximation, the phase shift in (11)

can be related to the deflection angle of the scattering orbits and used to compute the scattering amplitude. It turns out that the semiclassical results with a small spatially independent mass perturbation qualitatively agree with the full numerical studies in which the mass term is introduced to be space-dependent and vanishes in an asymptotic regime. This semiclassical analysis provides an alternative interpretation of the scattering cross section in terms of the orbiting.

The geodesics follows the spacetime with the line element of the form

$$ds^2 = - \left(1 - \frac{C^2 + D^2}{r^2}\right) dt^2 + \left(1 - \frac{D^2}{r^2}\right)^{-1} dr^2 - 2C d\phi dt + r^2 d\phi^2, \quad (14)$$

where $C = \ell/m_a c$ for the circulation of the vortex and $D = d/m_a c$ for the draining rate. The metric is independent of t and ϕ . There are two killing vectors leading to two conserved quantities, namely energy E and azimuthal angular momentum L , along a geodesic. In terms of the proper time τ [40–42], they are expressed by

$$E = \left(1 - \frac{C^2 + D^2}{r^2}\right) \frac{dt}{d\tau} + C \frac{d\phi}{d\tau}, \quad (15a)$$

$$L = -C \frac{dt}{d\tau} + r^2 \frac{d\phi}{d\tau}, \quad (15b)$$

giving two equations of motion

$$\frac{dt}{d\tau} = \frac{E - CL/r^2}{(1 - D^2/r^2)}, \quad (16a)$$

$$\frac{d\phi}{d\tau} = \frac{L}{r^2} + \frac{CE - LC^2/r^2}{r^2(1 - D^2/r^2)}. \quad (16b)$$

For the geodesics obeying $g_{\mu\nu} p^\mu p^\nu = -m^2 \equiv -\epsilon$ where $p^\mu = m dx^\mu/d\tau$ is the four-momentum, the radial motion can be derived as

$$\begin{aligned} \left(\frac{dr}{d\tau}\right)^2 &= \left(E - \frac{CL}{r^2}\right)^2 - \left(1 - \frac{D^2}{r^2}\right) \frac{L^2}{r^2} - \epsilon \left(1 - \frac{D^2}{r^2}\right) \\ &\equiv \left(\frac{dr^{(0)}}{d\tau}\right)^2 - \epsilon \left(1 - \frac{D^2}{r^2}\right). \end{aligned} \quad (17)$$

Here, we treat the mass term as a perturbation, that perturbs the null geodesics $r^{(0)}$. Hence, together with (16) and (17), the equation for radial motion up to order ϵ becomes

$$\frac{dr}{d\phi} = \frac{dr^{(0)}}{d\phi} - \frac{(1 - D^2/r^2)}{2(dr^{(0)}/d\tau)} \frac{1}{d\phi/d\tau} \epsilon + \mathcal{O}(\epsilon^2), \quad (18)$$

where the integral form of the deflection angle Θ shown

in Fig. 2 can be written as

$$\begin{aligned} \Theta &= -\pi + 2 \int_{r_0}^{\infty} \left| \frac{d\phi}{dr} \right| dr \\ &= -\pi + 2 \int_{r_0}^{\infty} \frac{d\phi}{dr^{(0)}} dr \\ &\quad - 2\epsilon \int_{r_0}^{\infty} \frac{(1 - D^2/r^2) (d\phi/d\tau)}{2(dr^{(0)}/d\tau)^3} dr + \mathcal{O}(\epsilon^2). \end{aligned} \quad (19)$$

The radial coordinate r_t is a turning point of the trajectory determined by $dr^{(0)}/d\tau = 0$ to be

$$C^2 b^2 - 2sC b r_t^2 E + D^2 b^2 - r_t^2 (b^2 - r_t^2 E^2) = 0 \quad (20)$$

with the impact parameter $b = \frac{|L|}{E}$ with $s = +/ -$ for co-rotating/counter-rotating orbits.

The radial velocity above for null geodesics takes the form

$$\frac{dr^{(0)}}{d\tau} \sim \frac{1}{r^2} \sqrt{(r - r_1)(r - r_2)(r - r_3)(r - r_4)}, \quad (21)$$

where we label the roots as $r_4 \geq r_3 > r_2 > r_1$, and the detailed expressions of the four roots can be seen in Appendix A in Ref. [41]. For the unstable circular motion, the radius r_{sc} is given by the double root $r_{sc} = r_3 = r_4$ with the corresponding critical impact parameter defined via (20).

It is straightforward to find the critical impact parameter b_{sc} given by [40, 42]

$$b_{\pm c} = 2\sqrt{D^2 + C^2} \mp 2C, \quad (22)$$

and the unstable circular orbits

$$r_{\pm c} = \left(\sqrt{D^2 + C^2} |b_{\pm c}|\right)^{1/2} \quad (23)$$

in Ref. [28]. Here we primarily focus on the large energy scattering when the impact parameter approaches the critical value, $b \rightarrow b_{sc} \propto r_E = \sqrt{D^2 + C^2}$ in the so-called strong deflection limit (SDL) [40, 42]. The leading behavior of the deflection angle in the SDL can be extracted from the integral in (19) in the region of $r \rightarrow r_t = r_{sc}$. Given by the inverse of the radial velocity in (21), in the case of the double root $r_{sc} = r_4 = r_3$, the first integral behaves like $1/(r - r_{sc})$ and the second integral of the ϵ correction results in the form $1/(r - r_{sc})^3$, giving the divergence at $r = r_t = r_{sc}$. Through the expansion of $b(r_t)$ around $r_t = r_{sc}$,

$$b(r_t) = b_{sc} + \frac{1}{2!} b''_{sc} (r_t - r_{sc})^2 + \mathcal{O}(r_t - r_{sc})^3, \quad (24)$$

where $b''_{sc} \equiv b''(r_{sc})$ and the prime means the derivative with respect to r_t , the divergence behavior can be translated into the form of $\log(b - b_{sc})$ and $(b - b_{sc})^{-1}$. As a result, the deflection angle in the SDL in terms of the impact parameter b is expressed as

$$\Theta^s(b) \approx -\bar{a}_s \log(b - b_{sc}) + \bar{b}_s + \frac{\epsilon}{E^2} \frac{\hat{a}_s}{(b - b_{sc})}, \quad (25)$$

with the coefficients

$$\bar{a}_s = \frac{r_{sc}}{2D} \left(\sqrt{1 + \frac{C^2}{D^2}} + \frac{sC}{D} \right), \quad (26)$$

$$\begin{aligned} \bar{b}_s = & -\frac{r_{sc}}{2D} \left(\sqrt{1 + \frac{C^2}{D^2}} + \frac{sC}{D} \right) \log \left(\frac{r_{sc}^2}{64b_{sc}(D^2 + C^2)} \right) \\ & - \frac{sC}{D} \log \left(\frac{r_{sc} + D}{r_{sc} - D} \right) - \pi \end{aligned} \quad (27)$$

in Ref. [28], and

$$\hat{a}_s = \frac{r_{sc}^3 [-C^2 b_{sc} + sC r_{sc}^2 + b_{sc} (r_{sc}^2 - D^2)]}{2(6C^2 b_{sc}^2 - 2sC b_{sc} r_{sc}^2 + 6D^2 b_{sc}^2 - b_{sc}^2 r_{sc}^2)^{3/2}}. \quad (28)$$

In Fig. 2, the deflection angle for the co-rotating orbit is given by

$$\Theta^+(b) = 2n\pi + \phi, \quad (29)$$

and for the counter-rotating is in particular defined as

$$\Theta^-(b) = 2n\pi - \phi, \quad (30)$$

where $0 < \phi < 2\pi$. Note that $n = 0$ ($n = 1$) is for the co-rotating (counter-rotating) orbit winding around the black hole zero time, which are two orbits contributing significantly to the semiclassical differential cross section to be discussed later [28]. One can write $b(\phi)$ by the inversion of (25) and with the deflection angle given by (29) and (30) as

$$b(\phi) = b_{sc} + b_s^{(0)}(\phi) + \frac{\epsilon}{E^2} b_s^{(1)}(\phi), \quad (31)$$

where

$$b_{\pm}^{(0)}(\phi) = \exp \left[\frac{-\bar{b}_{\pm} + 2n\pi \pm \phi}{-\bar{a}_{\pm}} \right], \quad (32)$$

and its correction of ϵ is

$$b_{\pm}^{(1)}(\phi) \approx \frac{\hat{a}_{\pm}}{\bar{a}_{\pm}}. \quad (33)$$

The classical differential cross section of the scattering is determined by the deflection angle

$$\left. \frac{d\sigma}{d\phi} \right|_{\text{cl}} = \left| \frac{d\Theta}{db} \right|^{-1}. \quad (34)$$

Quantum mechanically, the differential cross section can be computed from the scattering amplitude as in (13), where the scattering amplitude is given by the sum of the contributions of the scattered wave functions through their the phase shifts

$$f_{\omega}(\phi) \approx \sqrt{\frac{1}{2i\pi\omega}} \sum_{m=-\infty}^{\infty} e^{2i\delta_m} e^{im\phi} \quad (35)$$

in which the on-axis contributions are ignored [28]. The expression can be converted to the integral by the Poisson sum formula [39] as

$$\begin{aligned} f_{\omega}(\phi) = & \sqrt{\frac{1}{2i\pi\omega}} \sum_{n=-\infty}^{\infty} e^{-i\pi n} \int_{-\infty}^{\infty} dm e^{2i\delta_m} e^{im\phi} e^{2i\pi mn} \\ = & \sqrt{\frac{1}{2i\pi\omega}} \sum_{n=-\infty}^{\infty} \left[e^{-i\pi n} \int_{-\infty}^{\infty} dm e^{2i\delta_m} e^{im\phi} e^{2i\pi mn} \right. \\ & \left. + e^{i\pi n} \int_{-\infty}^{\infty} dm e^{2i\delta_{-m}} e^{-im\phi} e^{2i\pi mn} \right] \end{aligned} \quad (36)$$

Let us define

$$\xi_n^{\pm} = 2\delta_{\pm m(\phi)} \pm m\phi + 2\pi nm(\phi) \quad (37)$$

in terms of the phase shift $\delta_{\pm m}$ and $m(\phi)$, which can be linked to the orbital dynamics as $m(\phi) = \omega b(\phi)$ for fixed n . In the stationary phase condition,

$$\frac{d}{dm} \xi_n^{\pm} = \frac{d}{dm} [2\delta_{\pm m}] \pm \phi + 2n\pi = 0. \quad (38)$$

Then the phase shift can be related to the deflection angle in (29) and (30) as

$$\Theta^{\pm} = -\frac{d}{dm} (2\delta_{\pm m}), \quad (39)$$

and it can be analytically computed by integrating the deflection angle over $m = \omega b$. With the expression of the deflection angle in (25), the phase shift in the leading order of the SDL becomes

$$\begin{aligned} \delta_{\pm m} = & -\frac{\omega}{2} \int \Theta^{\pm}(b) db \\ \approx & -\frac{\omega}{2} \left\{ -\bar{a}_{\pm}(b - b_{\pm c}) \log(b - b_{\pm c}) + \bar{a}_{\pm}b + \bar{b}_{\pm}b \right. \\ & \left. + \frac{\epsilon}{E^2} \hat{a}_{\pm} \log(b - b_{\pm c}) \right\} \end{aligned}$$

Let us consider the contributions to the differential scattering cross section from two dominant contributions, $n = 0$ for the co-rotating orbit and $n = 1$ for the counter-rotating orbit. The total differential cross section can be approximated by the sum of the respective classical differential cross sections and their interference effect given by

$$\frac{d\sigma}{d\phi} \approx \frac{d\sigma^+}{d\phi} + \frac{d\sigma^-}{d\phi} + I. \quad (40)$$

where

$$\frac{d\sigma^{\pm}}{d\phi} = \left| \frac{d\Theta^{\pm}}{db} \right|^{-1} \approx \left| \frac{-\bar{a}_{\pm}}{b - b_{\pm c}} + \frac{\epsilon}{E^2} \frac{-\hat{a}_{\pm}}{(b - b_{\pm c})^2} \right|^{-1}, \quad (41)$$

and the interference term I between the two orbits is thus

$$I = 2 \left| \frac{d\Theta^+}{db} \frac{d\Theta^-}{db} \right|^{-1/2} \cos(\xi_0^+ - \xi_1^-). \quad (42)$$

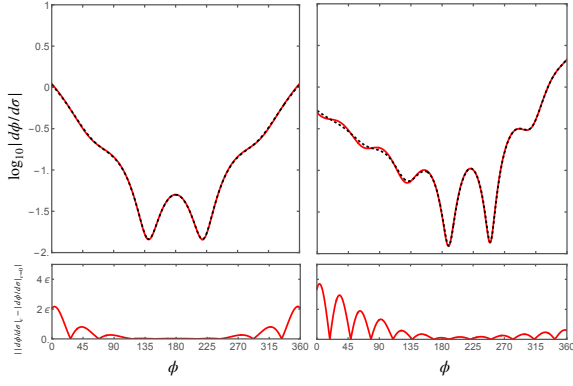


FIG. 3. Differential cross sections $d\sigma/d\phi$ as a function of scattering angle ϕ , showing contributions from the co-rotating orbit ($n = 0$) and the counter-rotating orbit ($n = 1$). Results are shown for $C = 0$ (left) and $C = 1$ (right), with frequency $\omega = 1$. The deviation of the scattering amplitude due to the perturbations as a function of the scattering angle is plotted.

Fig. 3 shows the deflection cross section in (42) with/without perturbations for non-rotating/rotating backgrounds. Based on (41), for the co-rotating (counter-rotating) orbit, the deflection angle of $0 < \phi < \pi$ ($\pi < \phi < 2\pi$) is with the impact parameter $b \gg b_{+c}$ ($b \gg b_{-c}$) where the inverse of $\frac{d\Theta^+}{db}$ ($\frac{d\Theta^-}{db}$) is large that dominates the total cross section at $0 < \phi < \pi$ ($\pi < \phi < 2\pi$). The interference term induces the oscillations with the wavelength in terms of ω and r_E as [28]

$$\lambda \approx \frac{\pi}{2\omega r_E} - \frac{\epsilon}{E^2} \left(\frac{\hat{a}_-}{\bar{a}_-} + \frac{\hat{a}_+}{\bar{a}_+} \right) \frac{\pi}{8\omega^2 r_E^2}, \quad (43)$$

where the mass perturbation shifts the wavelength of order ϵ also seen in Fig. 3. The detailed derivation can be seen in Appendix. Apart from that, the mass perturbation results in the relatively large modification of the differential cross section at the relatively small scattering angle due to the interference term I . This can be understood by the fact that the interference term involves the inverse of $\frac{d\Theta^+}{db}$ for the co-rotation orbit and $\frac{d\Theta^-}{db}$ for the counter-rotation orbit. At the scattering angle of $0 < \phi < \pi$ ($\pi < \phi < 2\pi$), the correction of order mass perturbation ϵ becomes evident arising from the large value of the inverse of the unperturbed $\frac{d\Theta^+}{db}$ ($\frac{d\Theta^-}{db}$) as $b \gg b_{+c}$ ($b \gg b_{-c}$). In addition, in the rotating background with $C = 1$, the effect of the perturbations to the scattering amplitude is more profound at the angle, of $0 < \phi < \pi$ as compared with the angle of $\pi < \phi < 2\pi$. In the expression of (41), the perturbed effect of $\frac{d\Theta}{db}$ is controlled by \hat{a}/\bar{a} with \bar{a} and \hat{a} given in (26) and (28) respectively. In general, $\bar{a}_- < \bar{a}_+$ due to $b_{-c} > b_{+c}$, which has been studied in Ref. [40] and it is also found that $\hat{a}_- > \hat{a}_+$, so that they lead to the large perturbed effect to the perturbed part of $\frac{d\Theta^-}{db}$. Through the interference term I , the perturbed effect is amplified again due to the largeness of the inverse of the unperturbed $\frac{d\Theta^-}{db}$ at the

angle of $0 < \phi < \pi$.

The cross section in the stationary phase approximation provides the qualitative feature of its full numerical result. In the numerical studies, the mass perturbation will be introduced to be space-dependent and then trigger the destabilization of the scattering amplitudes.

IV. REGEE POLES

In addition to the semiclassical treatment with a constant perturbation term, introducing a spatially dependent bump in the effective potential given by (8) allows us to model a more realistic situation in which a black hole is surrounded by environment matter. We numerically investigate the wave equation (7), where the solution obeys the boundary conditions of the pure ingoing wave at the horizon and the incoming/outgoing waves at infinity, expressed in (10). By further assuming that only the outgoing wave exists at infinity leads to $A^{\text{in}} = 0$ in (10) where one can have a spectrum of discrete complex-valued frequencies with a real-valued azimuthal numbers, the QMN, or complex-valued azimuthal numbers m with the real-valued frequencies, the RPs.

In scattering theory, the RPs can be used together with the CAM method to compute the scattering amplitude, as an alternative to the partial wave summation approach (11). Through the Watson transformation [43], the partial wave summation in (35) can be reformulated as a contour integral in the complex- m plane [28]

$$f_\omega(\phi) = \sqrt{\frac{1}{2i\pi\omega}} \left[\int_{-\infty}^{\infty} S(m) e^{im(\phi-2\pi)} dm + \frac{i}{2} \int_{-\infty+i\xi}^{\infty+i\xi} \frac{S(m) e^{im(\phi-\pi)}}{\sin m\pi} dm - \frac{i}{2} \int_{-\infty-i\xi}^{\infty-i\xi} \frac{S(m) e^{im(\phi-3\pi)}}{\sin m\pi} dm \right], \quad (44)$$

where ξ is a small real number, and $S(m) = ie^{im\pi} A^{\text{out}}/A^{\text{in}}$, with the poles when $A^{\text{in}} = 0$. For high frequencies, one can neglect the background contribution in the first term due to the absence of stationary phase point [28] and consider the contour enclosed in the upper half-plane for the second term, and in the lower half-plane for the last term, respectively. Then (44) can be further expressed as the sum of the residues (Res) of the RPs as

$$f_\omega(\phi) \approx -\sqrt{\frac{\pi}{2i\omega}} \sum_{n=0}^{\infty} \left[\frac{e^{im_{+n}(\phi-\pi)}}{\sin \pi m_{+n}} \text{Res}_{m \rightarrow m_{+n}} S(m) + \frac{e^{im_{-n}(\phi-3\pi)}}{\sin \pi m_{-n}} \text{Res}_{m \rightarrow m_{-n}} S(m) \right]. \quad (45)$$

Hence we can investigate the individual RP contributions to the scattering amplitude. It will be found below that summing up the contributions of sufficiently many dominant RPs can approximately reach the scattering amplitude by the partial wave summation.

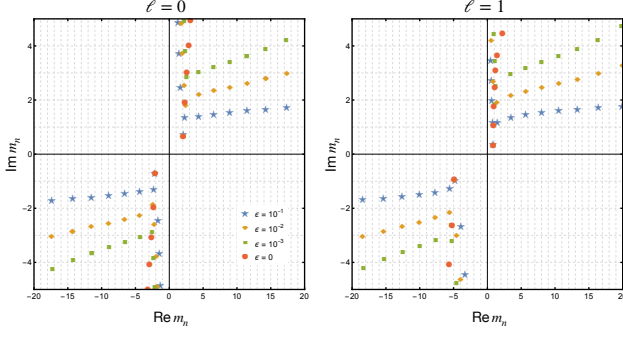


FIG. 4. The RP spectrum is shown under various perturbations in the non-rotating background ($\ell = 0$) in the left panel, and the rotating background ($\ell = 1$) in the right panel. The parameters are fixed at a frequency $\omega = 1.0$, and with the bump position $r_0 = 30$.

A. Regge pole spectrum and stability criterion against perturbations

We first compute the RPs with or without inhomogeneous mass perturbation (9) in both the non-rotating ($\ell = 0$) and rotating ($\ell = 1$) backgrounds using a modified continuous fraction method (see Appendix A). The resulting RP spectrum is shown in a complex- m plane in Fig. 4, where the filled red circles denote the unperturbed RPs, while other symbols correspond to the RPs with various values of the perturbations ϵ .

For $\ell = 0$, the spectrum exhibits symmetry between the co-rotating modes located at the upper right quadrant, namely $m_{\pm,n}^{(\epsilon)} = -m_{\mp,n}^{(\epsilon)}$, while for $\ell \neq 0$, the background rotation breaks this symmetric feature. The fundamental mode ($n = 0$) corresponds to the smallest absolute value of the imaginary part of m , i.e., $|\text{Im } m|$. Upon turning-on perturbations, the RP spectrum begins to bifurcate into two distinct branches: a inner branch with the poles characterized by smaller values of $|\text{Re } m_\omega|$ and an outer branch with the poles of the larger values of $|\text{Re } m_\omega|$. According to [29], the bifurcation in the RP spectrum is regarded as a sign of RP spectrum destabilization caused by the perturbations.

Fig. 4 shows that in general, the onset of bifurcation is located at the higher overtone given by smaller ϵ perturbations and moves toward the fundamental RP with relatively larger ϵ perturbations for both co- and counter-rotating modes. In the case of $\ell = 1$ of the rotating background, the bifurcation with $\epsilon = 10^{-3}$ starts between the third (second) overtone and the forth (first) overtone for the co-rotating (counter-rotating) modes and as the perturbation ϵ increases to $\epsilon = 10^{-1}$, it shifts toward the first overtone (fundamental RP). Thus, the co-rotating modes $m_{+,n}$ are more resistant to perturbations and tend to remain stable whereas the counter-rotating modes $m_{-,n}$ become susceptible to perturbations, to the extent that the onset of bifurcation shifts towards the fundamental

RP, resulting in destabilization. As the perturbation ϵ increases, the fundamental tone can become destabilized at a certain critical ϵ to be studied later. As in [44], which studied the QNMs in the associated pseudospectrum, it was also found that the prograde overtones become more stable than the retrograde overtones when they are perturbed in the rotating background.

For a fixed frequency ω , we quantitatively evaluate the modification of the RPs under the perturbations given by

$$\left| \frac{\lambda_{\pm,n}^{(\epsilon)} - \lambda_{\pm,n}^{(0)}}{\lambda_{\pm,n}^{(0)}} \right|_\omega = \left| \frac{\Delta \lambda_{\pm,n}^{(\epsilon)}}{\lambda_{\pm,n}^{(0)}} \right|_\omega, \quad n = 0, 1, 2, 3 \dots, \quad (46)$$

with $\lambda_{\pm,n}^{(\epsilon)} = m_{\pm,n}^{(\epsilon)} l$. Following the criterion in [36], the RP is considered as destabilized when the ratio $|\Delta \lambda_{\pm,n}^{(\epsilon)} / \lambda_{\pm,n}^{(0)}|$ is much larger than the perturbation ϵ . Conversely, when the ratio remains smaller than or the same order of ϵ , the poles are regarded as stable.

B. Migration of RP of overtones

To further explore the bifurcation spectrum, we consider the migration of the PRs by changing the bump position r_0 in (9) and focus on the large migration and the discontinuous overtaking jumps, both of which serves as strong indicators of destabilization [29, 36].

We zoom in on the poles of the second overtone of the co-rotating modes including the poles on the inner and outer branches as well as the first overtone in the left panel of Fig. 5 and track the trajectories of the poles starting from $r_0 = 10$. As the bump position increases from $r_0 = 10$ to 20, the pole of the second overtone in the outer branch reveals several overtaking jumps at approximately $r_0 = 12, 15$. The poles in the inner branch also have overtaking jumps at approximately $r_0 = 12, 15$, and 18. As for the first overtone, the spiral trajectory of the pole of the first overtone starts to bifurcate into two branches at $r_0 = 18$.

Remarkably, the onset of bifurcation shifts to the first overtone. Note that the same migration scheme where the onset of the bifurcation is shifted from the first overtone to the fundamental RP also applies to the counter-rotating modes. Therefore, the bifurcations and the consequent overtaking migrations in the complex- m plane can be regarded as a signature of RP destabilization

with large values of $\left| \frac{\Delta \lambda_{\pm,n}^{(\epsilon)}}{\lambda_{\pm,n}^{(0)}} \right|_\omega$, which can be as large as $\left| \frac{\Delta \lambda_{+,2}^{(\epsilon)}}{\lambda_{+,2}^{(0)}} \right|_\omega \approx 70\epsilon$ in the most right panel plot of Fig. 5 for the outer branch pole. The resulting impact on the scattering amplitude, particularly at large frequency, will be discussed later.

As for the low frequency case shown in Fig. 6, the bifurcation happens in the first overtone at $r_0 = 30$. Then, when r_0 increases to $r_0 = 90$, the pole in the

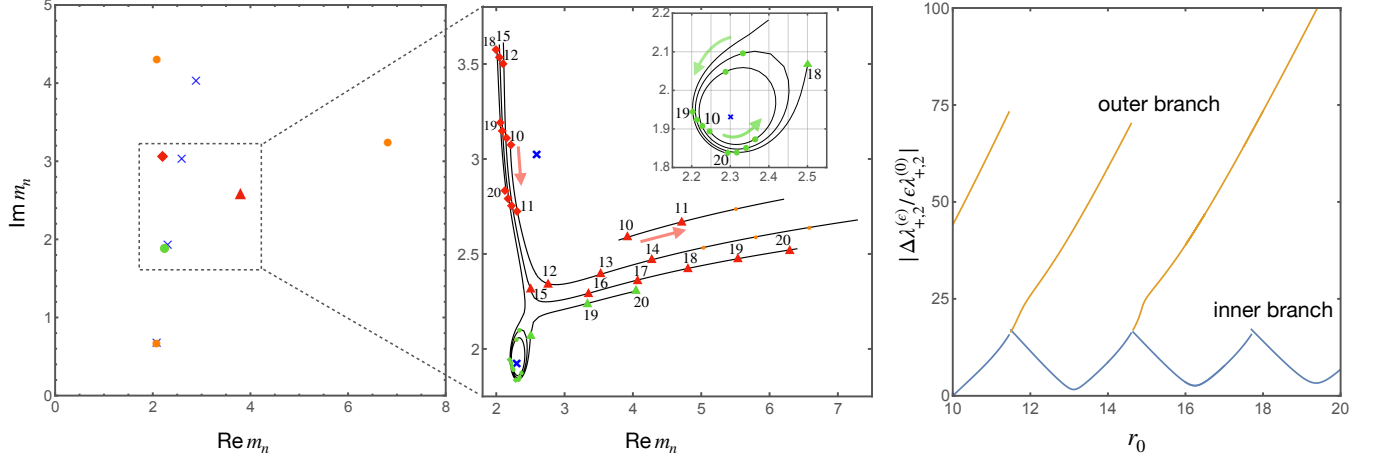


FIG. 5. Migration behavior for RPs illustrated by the case of $\ell = 0$ for high frequency as the bump position increases from $r_0 = 10$. In the left panel, we highlight the RP of the first overtone (blue cross) and the RPs of the bifurcated second overtone in the outer branch (red triangle) and inner branch (red square). In the middle panel, as r_0 increases, RPs have large migration or overtaking jump (as shown in the inset) signaling the shift of the bifurcation from the second overtone to the first overtone with the large $\left| \frac{\Delta\lambda_{+2}^{(\epsilon)}}{\lambda_{+2}^{(0)}} \right|_{\omega}$ in the right panel. Note that the spacing between adjacent red dots in the right panel is $\Delta r_0 = 1$.

outer branch undergoes overtaking jump again at $r_0 = 60$ where $\left| \frac{\Delta\lambda_{+1}^{(\epsilon)}}{\lambda_{+1}^{(0)}} \right|_{\omega} \approx 50\epsilon$. The pole in the inner branch also has another overtaking jump at $r_0 = 60$. At $r_0 = 90$, the fundamental RP bifurcates with the pole in its outer branch merging with the outer branch pole of the first overtone. From then, the onset of the bifurcation shifts from the first overtone to the fundamental RP. The destabilization of the poles will influence the scattering amplitude at relatively large scattering angles to be seen later.

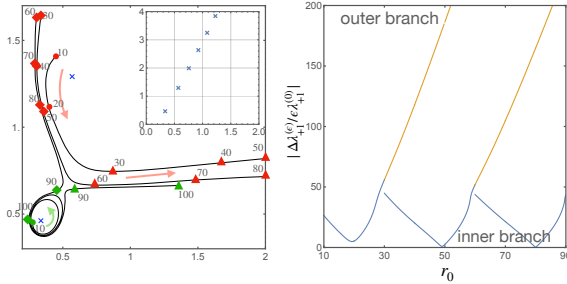


FIG. 6. Migration behavior for RPs illustrated by the case of $\ell = 0$ for low frequency as the bump position increases from $r_0 = 10$. Migration of the RP of the fundamental poles (blue triangle/square) and the RPs of the bifurcated first overtone in the outer branch (triangle red) and inner branch (square red), signaling the shift of the bifurcation from the first overtone to the fundamental pole. The inset shows the unperturbed RPs spectrum. The right panel is the values $|\Delta\lambda_{+1}^{(\epsilon)}/\epsilon\lambda_{+1}^{(0)}|$ for both the inner and outer branches as a functions of r_0 .

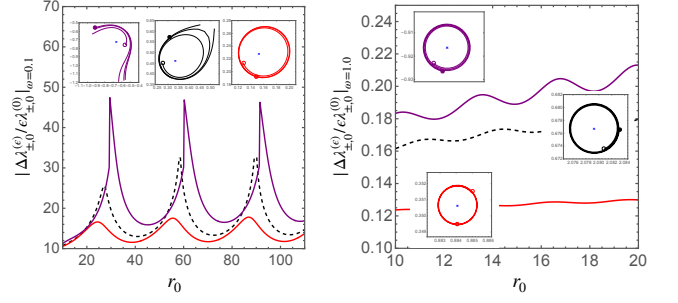


FIG. 7. The plots show the relative deviation $|\Delta\lambda_{\pm,0}^{(\epsilon)}/\lambda_{\pm,0}^{(0)}|$ of the fundamental RP as a function of r_0 where the purple (red) line is for the counter-rotating (co-rotating) case, and the black dashed line is for the non-rotating background with the results shown for frequencies $\omega = 0.1$ (left panel) and $\omega = 1.0$ (right panel).

C. Stability of the fundamental RP

We now focus on the fundamental RPs and track their trajectories in the complex- m plane as the bump position r_0 increases from 10 to 100, as depicted in Fig. 7. The figure shows in both non-rotating and rotating backgrounds, at low frequency, the quantity $|\Delta\lambda_{\pm,0}^{(\epsilon)}/\lambda_{\pm,0}^{(0)}|$ becomes large, indicating either significant migration or overtaking jumps in the pole trajectories. In contrast, at high frequencies, this ratio remains small and stable, and the pole migration follows a closed trajectory.

In particular, in the non-rotating background and at low frequency, the trajectory of the perturbed fundamental RP shows large migration at $r_0 \simeq 25$ and 55 , followed by an overtaking jump at $r_0 \simeq 90$, resulting

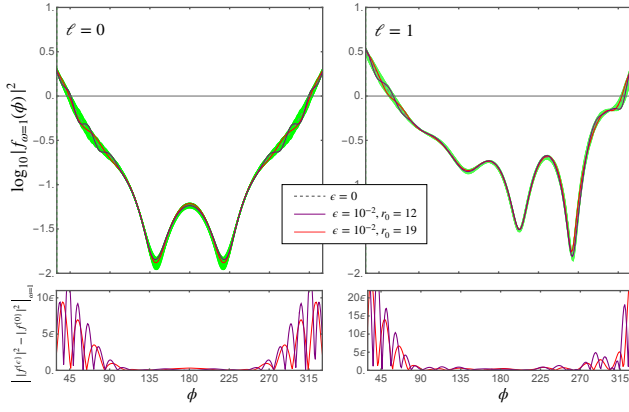


FIG. 8. The logarithm of the squared scattering amplitude is shown for low frequency $\omega = 1.0$ in the non-rotating (left) and the rotating (right) backgrounds, including both the unperturbed (blue curve) and perturbed cases. As the bump positions increases from $r_0 = 10$ to 20, the significant change is shown by the green shadow at relatively small scattering angles. The deviation of the scattering amplitude due to the perturbations as a function of the scattering angle is plotted.

in corresponding peaks of $|\Delta\lambda_0^{(\epsilon)}/\lambda_0^{(0)}|$. In the rotating background and also for low frequency, the trajectory of $m_{-,0}^{(\epsilon)}$ for the counter-rotating mode starts with the continuously spiral shift, and change to the discontinuously overtaking jump at $r_0 \simeq 30, 60$, and 95. These transitions lead to peaks into $|\Delta\lambda_{-,0}^{(\epsilon)}/\lambda_{-,0}^{(0)}|$, with values larger than those observed in the non-rotating background.

Conversely, regardless of the increase in r_0 , the migration of $m_{+,0}^{(\epsilon)}$ of the co-rotating mode remains in a closed trajectory with a relatively smaller value of $|\Delta\lambda_{+,0}^{(\epsilon)}/\lambda_{+,0}^{(0)}|$ than that of the non-rotating case. Again, for the fundamental RP in the rotating background, the co-rotating mode is more stable against the perturbations than the counter-rotating mode. The destabilization of the fundamental RP will influence the scattering amplitude in particular for low frequency at large scattering angles.

V. NUMERICAL STUDY OF SCATTERING CROSS SECTION

While the destabilized QNM spectrum has already been studied in the DBT under the environmental effect in Ref. [22], the instability there was demonstrated through time-dependent observables. Now we would like to study the observational consequence of RP destabilization mainly resulting from the spectrum bifurcation and pole migration by shifting the bump location r_0 .

To do so, we first numerically employs the partial wave summation method to obtain the scattering amplitude and the differential cross section under the perturbations, and compare the results to those of the unperturbed ones. As presented in Fig. 8 for relatively high frequency, the

effect of perturbations leads to an amplification of the oscillation amplitude in the differential cross section at small scattering angles, which can be qualitatively understood through semiclassical analysis due to the interference between the co-rotating and counter-rotating orbits, as shown in Fig. 3.

However, for inhomogeneous mass perturbations, the amplification is more effective and is seen resulting from the destabilization of the RPs, where the poles of the overtones in the outer branch reveal the large migration or overtaking jumps at some particular values of r_0 , as shown in Fig. 5, with which r_0 , the scattering amplitude has the peak values in Fig. 9. For $\ell = 1$ of the rotating background, the amplification mechanism is even more effective than in the $\ell = 0$ case of the non-rotating background at the scattering angle of $0 < \phi < \pi$, which also been seen in the semi-classical analysis in Fig. 3. Then, we employ the CAM method to try to understand the contributions of each pole branch to the scattering amplitude. In Fig. 10, for $\ell = 1$, the presence of the outer branch poles with $\text{Re } m_n > 0$ (co-rotating modes) and $\text{Re } m_n < 0$ (counter-rotating modes), together with the fundamental poles, contributes to the oscillatory pattern in the angular regions $0 < \phi < \pi$ and $\pi < \phi < 2\pi$, respectively. Similarly, for $\ell = 0$, the outer branch poles are also in charge of the oscillatory pattern. In addition, in the non-rotating background, contributions from the inner branch poles shift the scattering amplitude to a larger value, whereas in the rotating background, their effects are negligible.

As for low frequency, the scattering amplitude is shown in Fig. 11. For the unperturbed cases in both non-

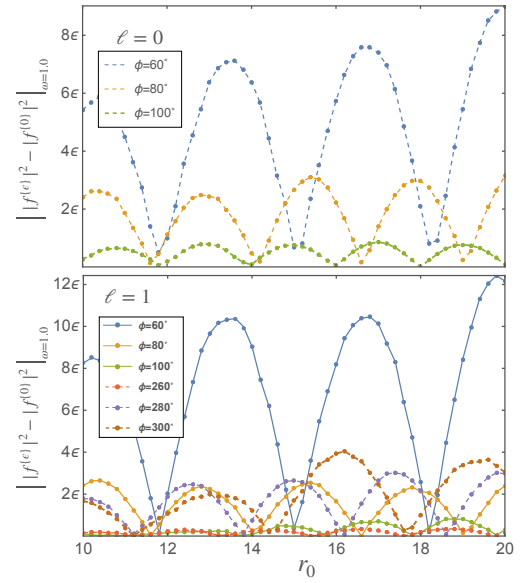


FIG. 9. The deviation of the scattering amplitude due to the perturbations for high-frequency in both the non-rotating (top) and rotating (bottom) backgrounds at various scattering angles.

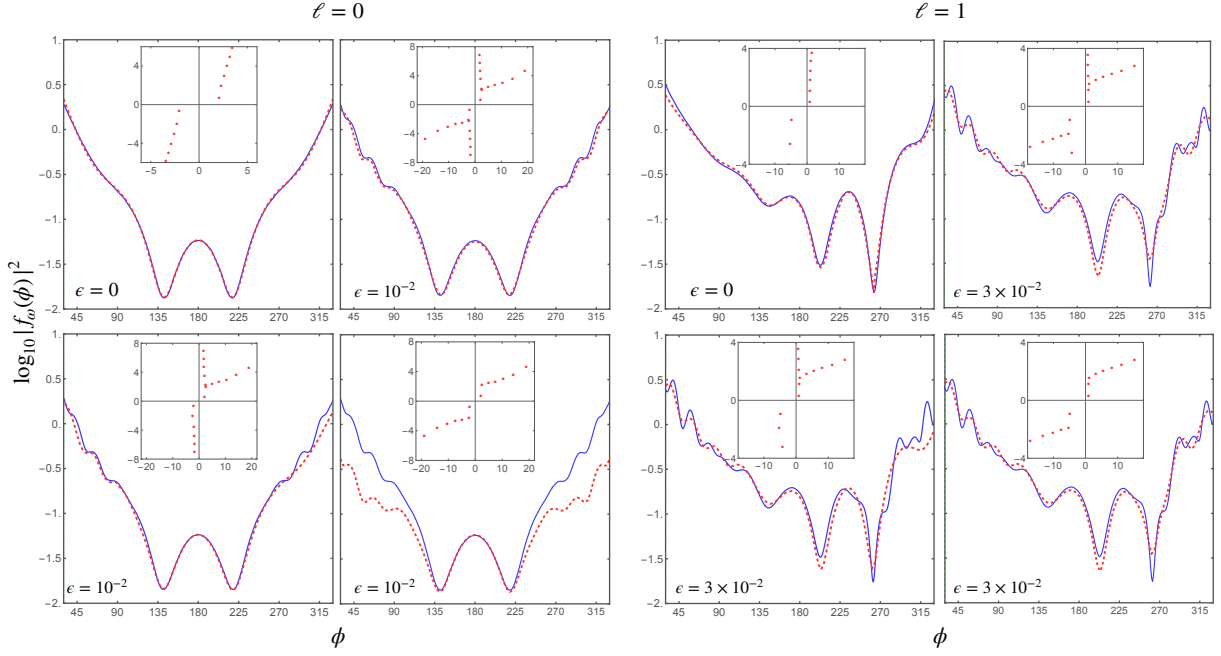


FIG. 10. Distinct pole branches contribute the scattering amplitude in their respective angular regions in both non-rotating and rotating backgrounds. In the cases of $\ell = 0$ and $\ell = 1$, the respective upper left plot is for the unperturbed scattering amplitude with the contributions of the RPs shown in the inset whereas the upper-right one is for the perturbed scattering amplitude with the contributions of the inner and outer pole branches. The lower-left plot is for the perturbed scattering amplitude with all contributions of the PRs but without the outer pole branch for $\text{Re } m_\omega < 0$. The lower-right plot is for the perturbed scattering amplitude with all contributions of the PRs but without the inner pole branch for $\text{Re } m_\omega > 0$.

rotating and rotating backgrounds, the scattering amplitudes are consistent with these reported in Ref. [28]. When turning on the space-dependence perturbations, the effects of the perturbations seem to give significant change in the scattering amplitude at all range of the scattering angles in Fig. 11. In principle, overtone destabilization in Fig. 6 leads to the large perturbed effects on the scattering amplitude at small scattering angles, whereas the fundamental RP destabilization in Fig. 7 leave an imprint on the scattering amplitude at large scattering angles, as summarized in Fig. 12. Notably, we have found that the fundamental RP is more stable in the co-rotating mode than in the counter-rotating mode, which is reflected the fact that the perturbed effect on the scattering amplitude is greater for $\phi \lesssim \pi$ compared to $\phi \gtrsim \pi$ (see Fig. 12). The overall effect can be seen in the scattering interference pattern in Fig. 13, where the perturbations induce a substantial effect at large angles, potentially observable in experiments.

VI. CONCLUDING REMARKS

In this article, we used a simple analogue system to study the resonance spectrum in terms of RPs, which could enhance our understanding of resonances in the

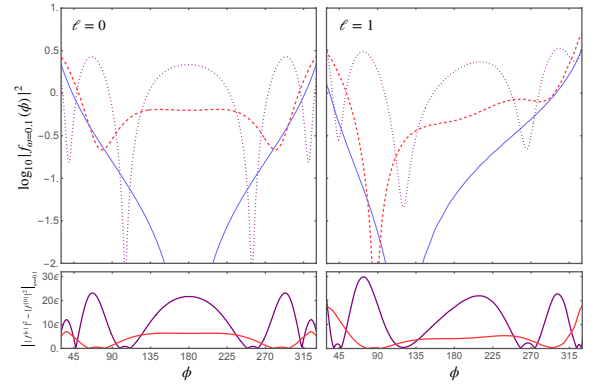


FIG. 11. The logarithm of the squared scattering amplitude is shown for low frequency $\omega = 0.1$ in the non-rotating (left) and the rotating (right) backgrounds, including both the unperturbed (blue curve) and perturbed cases. The red dashed line corresponds to $r_0 = 10$, while the purple dot-dashed line is for $r_0 = 30$.

context of a rotating black hole. We studied the destabilization of the RP spectrum and the associated observations of the scattering amplitude in the DBT geometry. We use a spatially tunable Rabi coupling in a two-component BEC system to study the gapped excitations

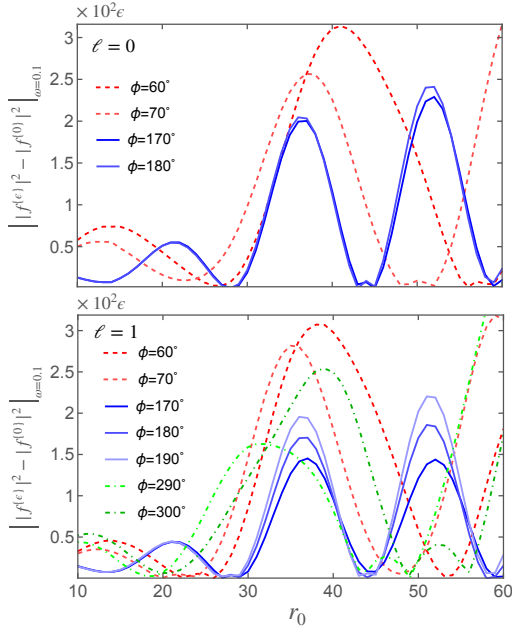


FIG. 12. The deviation of the scattering amplitude due to the perturbations for low frequency in both the non-rotating (top) and rotating (bottom) backgrounds at various scattering angles.

of the condensate. We consider the mass shell as a perturbation to mimic the environmental effects, giving a bump potential. We first compute the scattering amplitude with a homogeneous mass effect using the semiclassical approximation for high-frequency scattering to provide an alternative interpretation of the scattering amplitude in terms of orbiting, revealing clear signatures in the scattering amplitude.

A bifurcation in the RP spectrum occurs in the complex- m plane in the presence of a bump potential, which is an indicator of destabilization of the RP spectrum. When this occurs, the destabilization criterion, $|\Delta\lambda_{\pm,n}^\epsilon/\lambda_{\pm,n}^{(0)}| \gg \epsilon$ holds. Using the CAM method, it is demonstrated that the poles of the outer branch, together with the fundamental RP in the bifurcated spectrum, cause additional oscillations in the scattering amplitude. This contrasts with the interpretation derived from the semi-classical approximation. We also study the migration of RPs by shifting the bump position. Our results show that the RPs of the co-rotating modes are more stable than those of the counter-rotating modes. Large migrations and overtaking jumps of the overtones (fundamental RP) leave an imprint on the scattering amplitude at small (large) scattering angles. This effect can be observed in the scattering interference pattern in experiments.

Future research will investigate the static and dynamic tidal Love numbers in this draining bathtub model under the influence of the environment, as described in references [45–47]. This will help us understand the tidal responses of an analogue black hole, providing valuable

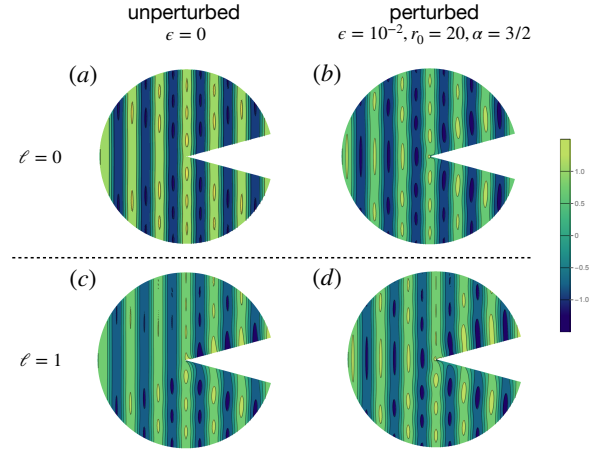


FIG. 13. The wave scattering interference patterns are shown for both unperturbed and perturbed cases. Planar waves with frequency $\omega = 0.1$ are incident from the left, and scattered by the analogue non-rotating ((a)-(b)) and rotating ((c)-(d)) black holes. In the perturbed case, the the magnitude of the large-angle scattering show the non-negligible difference from that of the unperturbed case. The blank region in the small angle is intentionally excluded to avoid numerical errors.

insights into related astrophysical phenomena.

ACKNOWLEDGMENTS

This work was supported in part by the National Science and Technology Council (NSTC) of Taiwan, Republic of China under the grant numbers 114-2112-M-160-001-MY2 (WCS) and 114-2112-M-259-007-MY3 (DSL).

Appendix A: Numerical method for computing Regge Poles.

For completeness, let us review the numerical method. The approach originated from [48], can be extended to the case of a mass shell around the black hole. We follow the numerical treatments of calculating the QNM and the RP spectrum for a black hole surrounded by thin-shell matter in Refs. [29, 30]. The solution of the Klein-Gordon equation (2) can be written as a series expansion around the point $r = b$ selected to be outside the mass shell where $b > r_0 + 1/\alpha$ in (9).

$$H_{\omega,m}(r) = e^{i\omega r^*(r)} \sum_{k=0}^{\infty} a_k \left(1 - \frac{b}{r}\right)^k. \quad (\text{A1})$$

After substituting it into the (2), we have four-term recurrence relation given by

$$\alpha_k a_{k+1} + \beta_k a_k + \gamma_k a_{k-1} + \delta_k a_{k-2} = 0, \quad (\text{A2})$$

for $k = 2, 3, \dots$, where

$$\alpha_k = -\frac{4(b^2 - 1)^2 k(k+1)}{b}, \quad (\text{A3})$$

$$\beta_k = \frac{8(b^2 - 1)k[-ib^3\omega + (b^2 - 3)k + 1]}{b}, \quad (\text{A4})$$

$$\begin{aligned} \gamma_k = & 6b[4k(2k-3) + 5] - \frac{5[4k(3k-5) + 9]}{b} \\ & - 4b(l^2 + 1)m^2 - 16ib^2(k-1)\omega \\ & + b^3[-4(k-1)k + 4m(2l\omega + m) - 1], \end{aligned} \quad (\text{A5})$$

$$\begin{aligned} \delta_k = & \frac{20(3-2k)^2}{b} + 8ib^2(k-2)\omega \\ & + 4b[-8k^2 + 22k + 2(l^2 + 1)m^2 - 15]. \end{aligned} \quad (\text{A6})$$

with the initial conditions

$$a_0 = e^{-i\omega r^*(b)} H_{\omega,m}(b), \quad (\text{A7})$$

$$a_1 = be^{-i\omega r^*(b)} \left[H'_{\omega,m}(r) - \frac{i\omega}{r^2 - 1} H_{\omega,m}(r) \right]_{r=b}, \quad (\text{A8})$$

which can be found numerically by integrating (2) from the horizon $r = 1$ up to $r = b > r_0 + 1/\alpha$.

Furthermore, one can use Gaussian elimination to re-

duce (A2) to the three-term recurrence relation

$$\alpha'_0 a_1 + \beta'_0 a_0 = 0, \quad (\text{A9})$$

$$\alpha'_k a_{k+1} + \beta'_k a_k + \gamma'_k a_{k-1} = 0, \quad k = 1, 2, \dots \quad (\text{A10})$$

α'_k, β'_k and γ'_k can be expressed in terms of $\alpha_k, \beta_k, \gamma_k$, and δ_k , given by

$$\alpha_0 = \alpha'_0, \beta'_0 = \beta, \gamma'_0 = \gamma_0 \quad (\text{A11})$$

$$\alpha_1 = \alpha'_1, \beta'_1 = \beta_1, \gamma'_1 = \gamma_1 \quad (\text{A12})$$

$$\begin{aligned} \alpha'_k &= \alpha_k, \beta'_k = \beta_k - \alpha'_{k-1} \delta_k / \gamma'_{k-1}, \quad \text{and} \\ \gamma'_k &= \gamma_k - \beta'_{k-1} \delta_k / \gamma'_{k-1}. \end{aligned} \quad (\text{A13})$$

Regarding to the issue of convergence of series expansion (S34), we refer the study of Ref. [49] where mentioned that a_k is a minimal solution to the recurrence relation when $b/2 < r_0 + 1/\alpha < b$ that in turn give the continued fraction as

$$\frac{a_1}{a_0} = -\frac{\gamma'_1}{\beta'_1 - \frac{\alpha'_1 \gamma'_2}{\beta'_2 - \frac{\alpha'_2 \gamma'_3}{\beta'_3 - \dots}}}. \quad (\text{A14})$$

This modified continued fraction method can calculate not only quasibound state but also the destabilized QNMs and RPs [36].

Appendix B: More detailed derivation of (43)

Here we provide more detailed derivations to achieve at (43). We start from the phase shift $\delta_{\pm m}$ and ξ_n^\pm ,

$$\begin{aligned} \xi_0^+ - \xi_1^- = & \omega \left\{ \bar{b}_- \left(e^{\frac{\bar{b}_- + \phi - 2\pi}{\bar{a}_-}} + b_{-c} \right) + \phi \left(e^{\frac{\bar{b}_- + \phi - 2\pi}{\bar{a}_-}} + b_{-c} \right) - 2\pi \left(e^{\frac{\bar{b}_- + \phi - 2\pi}{\bar{a}_-}} + b_{-c} \right) \right. \\ & + \bar{a}_- e^{-\frac{2\pi}{\bar{a}_-}} \left[e^{\frac{\bar{b}_- + \phi}{\bar{a}_-}} - e^{\frac{\bar{b}_- + \phi}{\bar{a}_-}} \log \left(e^{\frac{\bar{b}_- + \phi - 2\pi}{\bar{a}_-}} \right) + e^{\frac{2\pi}{\bar{a}_-}} b_{-c} \right] - \bar{b}_+ \left(e^{\frac{\bar{b}_+ - \phi}{\bar{a}_+}} + b_{+c} \right) \\ & + \phi \left(e^{\frac{\bar{b}_+ - \phi}{\bar{a}_+}} + b_{+c} \right) - \bar{a}_+ \left[e^{\frac{\bar{b}_+ - \phi}{\bar{a}_+}} - e^{\frac{\bar{b}_+ - \phi}{\bar{a}_+}} \log \left(e^{\frac{\bar{b}_+ - \phi}{\bar{a}_+}} \right) + b_{+c} \right] \Big\} \\ & + \omega \left[\frac{\hat{a}_- (\bar{b}_- + \phi - 2\pi)}{\bar{a}_-} + \frac{\hat{a}_+ (\phi - \bar{b}_+)}{\bar{a}_+} \right] \frac{\epsilon}{E^2} + \mathcal{O}(\epsilon^2). \end{aligned} \quad (\text{B1})$$

Then, the difference can be expanded as the following form

$$\xi_0^+ - \xi_1^- \approx (A + B\phi) + \frac{\epsilon}{E^2} (A' + B'\phi) + \mathcal{O}(\phi^2), \quad (\text{B2})$$

where the unperturbed terms with

$$\begin{aligned} A = & \omega \left[\bar{a}_- \left(e^{\frac{\bar{b}_- - 2\pi}{\bar{a}_-}} + b_{-c} \right) + \bar{a}_+ \left(-e^{\frac{\bar{b}_+}{\bar{a}_+}} - b_{+c} \right) + (\bar{b}_- - 2\pi)b_{-c} - \bar{b}_+ b_{+c} \right] \\ \approx & \omega(-2\pi b_{-c}) \\ \approx & -4\omega r_e \pi, \end{aligned} \quad (\text{B3})$$

$$\begin{aligned}
B &= \omega \left(b_{+c} + b_{-c} + e^{\frac{\bar{b}_- - 2\pi}{\bar{a}_-}} + e^{\frac{\bar{b}_+}{\bar{a}_+}} \right) \\
&\approx \omega(b_{+c} + b_{-c}) \\
&= 4\omega\sqrt{D^2 + C^2} \\
&= 4\omega r_e,
\end{aligned} \tag{B4}$$

and the perturbed terms with

$$\begin{aligned}
A' &= \omega \left[\frac{\hat{a}_-(\bar{b}_- - 2\pi)}{\bar{a}_-} - \frac{\hat{a}_+\bar{b}_+}{\bar{a}_+} \right], \\
B' &= \omega \left[\frac{\hat{a}_-}{\bar{a}_-} + \frac{\hat{a}_+}{\bar{a}_+} \right].
\end{aligned} \tag{B5}$$

Therefore, the wavelength is given by $B + \frac{\epsilon}{E^2} B' = 2\pi/\lambda$,

$$\lambda \approx \frac{\pi}{2\omega r_e} - \frac{\epsilon}{E^2} \left(\frac{\hat{a}_-}{\bar{a}_-} + \frac{\hat{a}_+}{\bar{a}_+} \right) \frac{\pi}{8\omega^2 r_e^2} \tag{B6}$$

with the small mass correction.

-
- [1] E. Berti, V. Cardoso, and A. O. Starinets, Quasinormal modes of black holes and black branes, *Classical and Quantum Gravity* **26**, 163001 (2009).
 - [2] R. A. Konoplya and A. Zhidenko, Quasinormal modes of black holes: From astrophysics to string theory, *Rev. Mod. Phys.* **83**, 793 (2011).
 - [3] A. Folacci and M. Ould El Hadj, Regge pole description of scattering of scalar and electromagnetic waves by a schwarzschild black hole, *Phys. Rev. D* **99**, 104079 (2019).
 - [4] E. Barausse, V. Cardoso, and P. Pani, Can environmental effects spoil precision gravitational-wave astrophysics?, *Phys. Rev. D* **89**, 104059 (2014).
 - [5] V. Cardoso and A. Maselli, Constraints on the astrophysical environment of binaries with gravitational-wave observations, *Astron. Astrophys.* **644**, A147 (2020).
 - [6] S. McGee, A. Sesana, and A. Vecchio, Linking gravitational waves and x-ray phenomena with joint lisa and athena observations, *Nature Astronomy* **4**, 26 (2020).
 - [7] V. Cardoso, I. P. Carucci, P. Pani, and T. P. Sotiriou, Black holes with surrounding matter in scalar-tensor theories, *Phys. Rev. Lett.* **111**, 111101 (2013).
 - [8] V. Cardoso, I. P. Carucci, P. Pani, and T. P. Sotiriou, Matter around kerr black holes in scalar-tensor theories: Scalarization and superradiant instability, *Phys. Rev. D* **88**, 044056 (2013).
 - [9] G. Lingetti, E. Cannizzaro, and P. Pani, Superradiant instabilities by accretion disks in scalar-tensor theories, *Phys. Rev. D* **106**, 024007 (2022).
 - [10] M. Visser, Acoustic black holes: horizons, ergospheres and hawking radiation, *Classical and Quantum Gravity* **15**, 1767 (1998).
 - [11] M. Richartz, A. Prain, S. Liberati, and S. Weinfurter, Rotating black holes in a draining bathtub: Superradiant scattering of gravity waves, *Phys. Rev. D* **91**, 124018 (2015).
 - [12] T. Torres, S. Patrick, A. Coutant, M. Richartz, E. W. Tedford, and S. Weinfurter, Rotational superradiant scattering in a vortex flow, *Nature Physics* **13**, 833 (2017).
 - [13] T. Torres, S. Patrick, M. Richartz, and S. Weinfurter, Quasinormal mode oscillations in an analogue black hole experiment, *Phys. Rev. Lett.* **125**, 011301 (2020).
 - [14] A. Berti, L. Giacomelli, and I. Carusotto, Superradiant phononic emission from the analog spin ergoregion in a two-component bose-einstein condensate, *C. R. Physique* **24**, 1 (2023).
 - [15] S. Patrick, A. Geelmuyden, S. Erne, C. F. Barenghi, and S. Weinfurter, Quantum vortex instability and black hole superradiance, *Phys. Rev. Res.* **4**, 033117 (2022).
 - [16] U. R. Fischer and R. Schützhold, Quantum simulation of cosmic inflation in two-component bose-einstein condensates, *Phys. Rev. A* **70**, 063615 (2004).
 - [17] S. Liberati, M. Visser, and S. Weinfurter, Naturalness in an emergent analogue spacetime, *Phys. Rev. Lett.* **96**, 151301 (2006).
 - [18] M. Visser and S. Weinfurter, Massive klein-gordon equation from a bose-einstein-condensation-based analogue spacetime, *Phys. Rev. D* **72**, 044020 (2005).
 - [19] W.-C. Syu, D.-S. Lee, and C.-Y. Lin, Analogous hawking radiation and quantum entanglement in two-component bose-einstein condensates: The gapped excitations, *Phys. Rev. D* **106**, 044016 (2022).
 - [20] W.-C. Syu and D.-S. Lee, Analogous hawking radiation from gapped excitations in a transonic flow of binary bose-einstein condensates, *Phys. Rev. D* **107**, 084049 (2023).
 - [21] W.-C. Syu, D.-S. Lee, and C.-Y. Lin, Analogue stochastic gravity phenomena in two-component bose-einstein condensates: Sound cone fluctuations, *Phys. Rev. D* **99**, 104011 (2019).
 - [22] W.-C. Syu and D.-S. Lee, Acoustic quasibound states and tachyonic instabilities from binary bose-einstein conden-

- sates, *Phys. Rev. D* **110**, 044017 (2024).
- [23] J. H. Kim, D. Hong, and Y. Shin, Observation of two sound modes in a binary superfluid gas, *Phys. Rev. A* **101**, 061601 (2020).
- [24] R. Cominotti, A. Berti, A. Farolfi, A. Zenesini, G. Lamporesi, I. Carusotto, A. Recati, and G. Ferrari, Observation of massless and massive collective excitations with faraday patterns in a two-component superfluid, *Phys. Rev. Lett.* **128**, 210401 (2022).
- [25] C. Hamner, J. J. Chang, P. Engels, and M. A. Hoefer, Generation of dark-bright soliton trains in superfluid-superfluid counterflow, *Phys. Rev. Lett.* **106**, 065302 (2011).
- [26] C. Hamner, Y. Zhang, J. J. Chang, C. Zhang, and P. Engels, Phase winding a two-component bose-einstein condensate in an elongated trap: Experimental observation of moving magnetic orders and dark-bright solitons, *Phys. Rev. Lett.* **111**, 264101 (2013).
- [27] S. R. Dolan, L. A. Oliveira, and L. C. B. Crispino, Resonances of a rotating black hole analogue, *Phys. Rev. D* **85**, 044031 (2012).
- [28] S. R. Dolan and E. S. Oliveira, Scattering by a draining bathtub vortex, *Phys. Rev. D* **87**, 124038 (2013).
- [29] T. Torres, From black hole spectral instability to stable observables, *Phys. Rev. Lett.* **131**, 111401 (2023).
- [30] T. Torres, M. O. E. Hadj, S.-Q. Hu, and R. Gregory, Regge pole description of scattering by dirty black holes, *Phys. Rev. D* **107**, 064028 (2023).
- [31] T. A. S. Cardoso and M. Richartz, Dissipative quantum vortices and superradiant scattering, *Phys. Rev. A* **106**, 063310 (2022).
- [32] C. J. Myatt, E. A. Burt, R. W. Ghrist, E. A. Cornell, and C. E. Wieman, Production of two overlapping bose-einstein condensates by sympathetic cooling, *Phys. Rev. Lett.* **78**, 586 (1997).
- [33] D. S. Hall, M. R. Matthews, J. R. Ensher, C. E. Wieman, and E. A. Cornell, Dynamics of component separation in a binary mixture of bose-einstein condensates, *Phys. Rev. Lett.* **81**, 1539 (1998).
- [34] S. B. Papp, J. M. Pino, and C. E. Wieman, Tunable miscibility in a dual-species bose-einstein condensate, *Phys. Rev. Lett.* **101**, 040402 (2008).
- [35] S. Tojo, Y. Taguchi, Y. Masuyama, T. Hayashi, H. Saito, and T. Hirano, Controlling phase separation of binary bose-einstein condensates via mixed-spin-channel feshbach resonance, *Phys. Rev. A* **82**, 033609 (2010).
- [36] M. H.-Y. Cheung, K. Destounis, R. P. Macedo, E. Berti, and V. Cardoso, Destabilizing the fundamental mode of black holes: The elephant and the flea, *Phys. Rev. Lett.* **128**, 111103 (2022).
- [37] A. Courty, K. Destounis, and P. Pani, Spectral instability of quasinormal modes and strong cosmic censorship, *Phys. Rev. D* **108**, 104027 (2023).
- [38] K. W. Ford and J. A. Wheeler, Semiclassical description of scattering, *Annals of Physics* **7**, 259 (1959).
- [39] H. M. Nussenzweig, *Diffraction Effects in Semiclassical Scattering*, Montroll Memorial Lecture Series in Mathematical Physics (Cambridge University Press, 1992).
- [40] T. Hsieh, D.-S. Lee, and C.-Y. Lin, Strong gravitational lensing by kerr and kerr-newman black holes, *Phys. Rev. D* **103**, 104063 (2021).
- [41] C.-Y. Wang, D.-S. Lee, and C.-Y. Lin, Null and timelike geodesics in the kerr-newman black hole exterior, *Phys. Rev. D* **106**, 084048 (2022).
- [42] T. Hsieh, D.-S. Lee, and C.-Y. Lin, Throat effects on strong gravitational lensing in kerr-like wormholes, *Phys. Rev. D* **111**, 044051 (2025).
- [43] R. G. Newton, *Scattering Theory of Waves and Particles* (Springer Berlin, Heidelberg, 1982).
- [44] L. T. de Paula, P. H. C. Siqueira, R. P. Macedo, and M. Richartz, *Pseudospectrum of rotating analogue black holes* (2025), [arXiv:2504.00106 \[gr-qc\]](https://arxiv.org/abs/2504.00106).
- [45] V. De Luca, B. Khek, J. Khoury, and M. Trodden, Tidal love numbers of analog black holes, *Phys. Rev. D* **111**, 044069 (2025).
- [46] L. Hui, A. Joyce, R. Penco, L. Santoni, and A. R. Solomon, Static response and love numbers of schwarzschild black holes, *Journal of Cosmology and Astroparticle Physics* **2021** (04), 052.
- [47] S. Chakraborty, E. Maggio, M. Silvestrini, and P. Pani, Dynamical tidal love numbers of kerr-like compact objects, *Phys. Rev. D* **110**, 084042 (2024).
- [48] E. W. Leaver, Quasinormal modes of reissner-nordström black holes, *Phys. Rev. D* **41**, 2986 (1990).
- [49] O. Benhar, E. Berti, and V. Ferrari, The imprint of the equation of state on the axial w-modes of oscillating neutron stars, *Monthly Notices of the Royal Astronomical Society* **310**, 797 (1999), <https://academic.oup.com/mnras/article-pdf/310/3/797/3135284/310-3-797.pdf>.